

Daily Evapotranspiration Estimation Using HJ-1 Data for Irrigation Water Management in a Desert-Oasis Irrigation District, Northwest China

Zhenyan Yi¹, Yunzhong Jiang¹, Hongli Zhao^{1a}, Haichen Li², Rong Wang^{1,3}, Pengcheng Huang^{1,3}

¹Department of Water Resources, China Institute of Water Resources and Hydropower Research, 100038, Beijing, China

²State Key Laboratory of Simulation and Regulation of Water Cycle in River Basin, China Institute of Water Resources and Hydropower Research, 100038, Beijing, China

³Faculty of Geomatics, Lanzhou Jiaotong university, 730070, Lanzhou, China

Abstract. Irrigation of agricultural land is the main water consumer in the arid and semiarid regions. The accurate time series of daily evapotranspiration (ET) at the field scale is crucial for irrigation water management. Here, we presented an integrated approach to field-scale ET mapping by combing METRIC (Mapping Evapotranspiration at High Resolution with Internalized Calibration) with trapezoidal framework of vegetation fraction and land surface temperature (f_v - T_{rad}). This approach fed with Chinese satellite HJ-1 (environmental and disaster monitoring and forecasting with a small satellite constellation) images was used to map daily ET over the desert-oasis irrigation fields in the middle of the Heihe River Basin, Northwest China. The results showed that time series of daily ET derived from HJ-1 were well consistent with the *in situ* measurements (coefficient of determination (R^2) of 0.95, root mean square error (RMSE) of 0.31 mmd^{-1} , mean absolute percentage error (MAPE) of 12.0% at Daman station; R^2 of 0.89, RMSE of 0.16 mmd^{-1} , and MAPE of 13.2% at Huazhaizi station). The rapid variation of ET could be precisely captured by HJ-1, especially when rainfall or irrigation events occurred between successive acquisitions of satellite data. Meanwhile, the spatiotemporal variation of monthly ET is closely related to crop growth. Daily ET at field scale will support a variety of local interests in water use and irrigation management for both planning and regulatory purposes.

1 Introduction

Agriculture heavily relies on irrigation of water drawn from rivers or aquifer in arid and semiarid areas. In the past 50 years, the river runoff showed the declining trend with the change in intensive climate. But water consumption increases due to booming socio-economy and fast-growing population, which will further deteriorate the water resource status in China [1]. Evapotranspiration (ET), the total amount of land surface evaporation and plant transpiration, is the most active process in the terrestrial hydrological cycle and the major component of energy and water balance in agricultural system. In the north of China, agricultural water consumption accounts for about 70% of total water consumption, and more than 90% of agricultural water is consumed via ET [2]. Therefore, it is necessary to determine the accurate spatiotemporal ET in irrigated fields for recognizing the crop consumption patterns, evaluating water use efficiency and optimizing irrigation scheduling, especially in the semi-arid and arid areas.

Typically, ground observation systems including lysimeters, Bowen ratio systems, eddy covariance systems (EC), and large aperture scintillometers are considered to be accurate for measure ET at individual

sites or for small footprint [3-5]. However, these observation systems are not applicable to a large region due to their high cost. New approaches to take advantage of remote sensing (RS) to map ET have been developed, especially in recent decades. Major improvements in ET estimates have been obtained through RS methods based on thermal infrared (TIR) data. A suite of algorithms that were based on surface residual of the energy balance, derived from optical and TIR observations, has been extensively developed and applied. One-source models include surface energy balance algorithm for land (SEBAL) [6], surface energy balance system (SEBS) [7], mapping evapotranspiration at high resolution with internalized calibration (METRIC) [8], and simplified surface energy balance (SSEB) [9]. Two-source models, such as the two-source energy balance model (TSEB) [10] and the disaggregated atmosphere-land exchange inverse (DisALEXI) [11], integrate the biophysical processes and RS data to estimate the plant transpiration and evaporation from non-vegetated surfaces separately. As reported in several reviews (e.g., Kalma et al., 2008; Liang et al., 2010), these approaches appear to accurately reproduce ET over a wide range of conditions at both the satellite overpass time and daily time scales [12,13]. Here we selected METRIC algorithm to

^a Corresponding author: zhaohl@iwhr.com

estimate the field evapotranspiration. METRIC algorithm evolved from SEBAL but uses ground-based meteorological measurements of reference ET acquired within scene to establish the latent heat flux at the cold pixel, rather than assuming a priori that sensible heat flux equals zero for the condition. This innovation makes the best use of existing technology in agricultural areas and establishes a “reality check” for the satellite-based ET estimates, which makes it more robust [14]. It performed well in estimating high-resolution ET with the relative errors of 10%-30% at different ecosystems around the world [15-17].

Local scale water management usually requires temporally continuous high spatial resolution ET in order to understand the crops ET variation, which is related to spatial heterogeneity in crop type, phenological stage, meteorological conditions, as well as soil moisture conditions [18]. The 100-m resolution characteristic of TIR imagery such as Landsat series, which we define as “moderate resolution” to distinguish from the high-resolution (meter scale) shortwave imagery collected by the Landsat series of satellites has proven critical to many operational needs for ET data because it will typically enable discrimination of individual agricultural fields [19]. But moderate resolution cannot realize the temporally continuous daily ET data because of the long revisit period and cloud contamination [20]. The Chinese Environment and Disaster Monitoring and Forecasting with a Small Satellite Constellation (HJ-1) can provide global coverage every two days with a spatial resolution of 30 m, which makes it a good balance of temporal and spatial resolution. The characteristics of short repeat interval and high spatial resolution are very useful for monitoring the regional land surface variables, such as vegetation indexes (VI), drought indexes, land surface temperature (LST), and ET [21-23].

Here METRIC fed with HJ-1 data was applied in the middle reach of Heihe River Basin to estimate daily ET at field scale for irrigation water management in 2015. A trapezoidal framework of vegetation and land surface temperature ($f_c - T_{rad}$) was integrated into METRIC to reduce ambiguity and uncertainty in the latent heat flux estimation due to the differing extremes possibly selected by the operator. The main objectives of this paper were to: 1) obtain and validate continuous daily ET at field scale through METRIC model driven by HJ-1 data; 2) characterize the spatial and temporal variations of ET values for different land cover types.

2 Materials and Methods

2.1 Experimental Region and Data

2.1.1 Study Area

Heihe River Basin (HRB) is the second largest inland river basin in the arid region of northwest China. The experimental area (100.03°-100.68° E, 38.33°-39.2° N) including Daman, Yingke, Ganjun, Shangshan, Wujiang

and Xigan irrigation districts is located in the middle reaches of HRB, as shown in Figure 1. The study area has a continental, dry, temperate climate with a mean annual temperature, precipitation, and open water evaporation of 7.6 °C, 116.8 mm, and 2390.0 mm, respectively [24]. During the growth period, the crop needs much water and irrigation is required in these months to meet crop growth requirements. Take 2012 as example, irrigation for oasis agriculture in the middle of HRB consumed 10.6×10^8 m³ of surface water diverted from Heihe River and 5.36×10^8 m³ from pumped groundwater [25]. Ganzhou irrigation district is an important maize seed production base in Northwest China. Maize is predominant crop in the irrigation districts. Other plants include spring wheat, alfalfa, cotton, woods, vegetables and fruits.

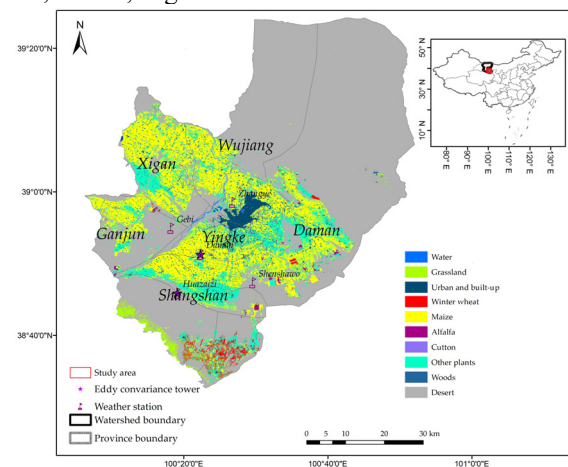


Figure 1. Location of study area and observations.

2.1.2 Fields Measurement

There are five ground observation stations in the study area: Daman, Huazhaizi, Shenshawo, Zhangye and Gobi. An automatic weather station (AWS) was installed at each site and equipped with sensors for collecting data including temperature, wind speed and direction, air pressure, humidity, precipitation, soil moist profile, solar radiation, four-component radiation, soil heat flux, and infrared temperature every 10 min over the whole year of 2015. Daman Station and Huazhaizi Station were also equipped with an eddy covariance (EC) system. The EC sensors were installed at the height 4.5 m above the ground. All EC data were sampled at a frequency of 10 Hz and turbulent fluxes (sensible heat flux and latent heat flux) were recorded every 30 min. The Gaussian fitting method was used to interpolate the missing data (Xu et al., 2017) [26]. In the case of the energy balance of EC system, the closure error of EC-based measurements at the daily scale was calculated based on the energy balance ratio (EBR) to correct the daily flux data (Liu et al., 2011) [27].

2.1.3 Satellite Data

HJ-1 was launched by the China Center for Resources Satellite Data and Applications (CRESDA) on September 6, 2008. There are two optical charge coupled

devices (CCDs) and a hyper-spectrum image (HIS) loaded on HJ-1A, and there are two CCDs and an infrared scanner (IRS) on HJ-1B. HJ-1 can provide visible/near-infrared/thermal/infrared (VIS/NIR/TIR) images with 30 m, 150 m, and 300 m spatial resolution respectively, with every 2-4 days' revisit time covering China and the surrounding areas. Based on the consideration of the satellite image quality of the HJ-1 and Landsat 8, the 36 available HJ-1 images and 9 available Landsat 8 images obtained in the growth season of 2015 from April to October were selected. All the images were subjected to geometric correction and atmospheric correction.

A DEM (30m) covering Heihe River Basin was provided by the "Heihe Plan Science Data Centre, National Natural Science Foundation of China" (<http://www.heihedata.org>). DEM data were used to demonstrate the terrain of the study area and applied in METIRC. Cropping pattern data were derived from HJ-1 and Landsat 8 data with support vector machine (SVM), object-based method, and time-series analysis to improve the classification accuracy and the overall accuracy for the crop classification reached 84% [28].

2.2 Methodology

2.2.1 Brief Outline of METRIC Algorithm

METRIC is a one-source model, which considers soil and vegetation as a sole source in the estimation of ET. It is widely used to estimate daily ET at the field scale. The latent heat flux (λET) is computed as a residual of the energy balance equation on a pixel by pixel basis:

$$\lambda ET = R_n - G - H \quad (1)$$

where R_n is net surface radiation, G is soil heat flux and H is sensible heat flux. Their units are all Wm^{-2} . Each energy component in Equation 1 can be calculated as follows:

$$R_n = (1 - \alpha)R_s \downarrow + R_L \downarrow - R_L \uparrow - (1 - \varepsilon)R_L \downarrow \quad (2)$$

$$G = (0.05 + 0.18e^{-0.52LAI})R_n (LAI \geq 0.5) \quad (3)$$

$$G = \left(\frac{1.8(T_{rad} - 273.16)}{R_n} + 0.084 \right) R_n (LAI < 0.5) \quad (4)$$

$$H = \frac{\rho_{air} C_p dT}{r_{ah}} \quad (5)$$

Where $R_{s\downarrow}$ is the down-welling shortwave radiation (Wm^{-2}); $R_{L\downarrow}$ is the down-welling long wave radiation (Wm^{-2}); $R_{L\uparrow}$ is the up-welling longwave radiation (Wm^{-2}); α is the surface albedo for shortwave radiation; ε is broad band surface emissivity; T_{rad} is the surface radiometric temperature (K); LAI is leaf area index; ρ_{air} is air density (kgm^{-3}); C_p is air specific heat at constant pressure ($1004 Jkg^{-1}K^{-1}$); r_{ah} is the aerodynamic resistance to heat transport (sm^{-1}); and dT represents the near surface to air temperature difference (K). dT is assumed to have a linear relationship with land surface temperature (Equation 6) as developed by Bastiaanssen et al. (1998) [6].

$$dT = aT_{rad} + b \quad (6)$$

In METRIC, an iterative method was applied to calculate both r_{ah} and H to reduce the effects of buoyancy of heated, light air at the surface. The algorithm started with finding a set of "hot" and "cold" pixels. It assumed that λET equals to 0.05 and 1.05 times reference ET (ET_0) for "hot" and "cold" pixels at the beginning of the iteration, and then calculated dT_{hot} and dT_{cold} , followed by calculating a and b , and then updating dT , and H . The Monin–Obuknov length (L) was used to define the stability conditions of the atmosphere during iteration in METRIC. The iteration stops when the value of r_{ah} remains stable. It is critically important to note that METRIC or all studies pertaining to SEBAL, recognize the key role of extremes in the resulting estimates [29]. A large uncertainty in the model outputs could be introduced by differing extremes manually identified by the operator. Here we introduced a trapezoid framework of $f_c T_{rad}$ to replace the intractable step of the selection of two extremes.

Instantaneous ET (ET_{inst}) of each pixel at satellite overpass time is calculated from Equation 1-6. It is extended to daily values (ET_{daily}) by fraction of reference ET (ET_0F) in METRIC, which is calculated by dividing ET_{inst} by hourly reference ET (ET_{0_inst}). It is assumed that the value of instantaneous ET_0F is the same as the average value within 24 h of the day satellite overpass. Finally, the daily ET at each pixel is calculated as a product of ET_0F and daily ET_0 :

$$ET_0F = \frac{ET_{inst}}{ET_{0_inst}} \quad (7)$$

$$ET_{daily} = ET_0F ET_{0_daily} \quad (8)$$

More details about METRIC algorithm can be found in Allen et al. (2007) [8]. Irrigation management requires continuous daily ET especially during growth seasons so that ET losses can be compensated by applying the proper quantity of water at the right time to meet the water demands of plants. Continuous daily ET can be derived from a series of ET_0F images by interpolating ET_0F between processed images and multiplying, on a daily basis, by the ET_0 for each day. Here we applied a cubic spline interpolation method to generate a smoothed ET_0F curve based on the nonlinearity of the temporal dynamics of ET_0F [30]. Then continuous daily ET was derived from the smoothed curve and multiplied by daily ET_0 (ET_{0_daily}).

2.2.2 Brief Outline of METRIC Algorithm

METRIC is set by some training and manual image interpretation of a hot and cold pixel to determine the temperature difference (dT) between the surface and the lower atmosphere, which is assumed to be linearly correlated with land surface temperature throughout a scene. Coefficients a and b are determined by the characteristic variables for two anchor points selected from the satellite image. The hot anchor pixel is selected where bare land is assumed to be dry enough and ET could be assumed to zero. The cold anchor pixel is selected among the open water or well-watered, full-

cover vegetation area, where the surface temperatures are shown to be considerably low. At the cold pixel, the available energy almost goes to ET, whereas H and dT are both assumed to be near zero. In terms of these definition, a and b can be expressed as:

$$a = \frac{r_{ah,hot}}{\rho_{hot} C_p} \frac{R_{n,hot} - G_{hot}}{T_{rad,hot} - T_{rad,cold}} \quad (9)$$

$$b = -aT_{rad,cold} \quad (10)$$

The variables in Equation 9 and 10 are the corresponding variables in Equation 5 and 6 for hot or cold extremes. In this study, to reduce the arbitrariness caused by the subjectivity in the selection of hot and cold pixels, a method based on the trapezoidal framework of the temperature-vegetation index space (f_c - T_{rad}) proposed by Long and Singh (2012) was introduced [31]. It is assumed that the coefficients a and b vary with f_c but remain fairly invariant under the same f_c or within the same f_c class:

$$a_i = \frac{r_{ah,hot,i}}{\rho_{hot,i} C_p} \frac{R_{n,hot,i} - G_{hot,i}}{T_{rad,hot,i} - T_{rad,cold,i}} \quad (11)$$

$$b_i = -a_i T_{rad,cold,i} \quad (12)$$

where subscript i denotes class i of f_c . The other variables in Equation (10) and (11) are the corresponding variables for hot or cold extremes. Pixel with the same f_c value or within class $f_{c,i}$, use a_i and b_i to infer their temperature gradient dT_i . The detailed calculation of f_c - T_{rad} space could be found in Long and Singh (2012) [31].

3 Results and Discussions

3.1. Evaluating the Performance of Continuous Daily ET Estimates from HJ-1

The continuous daily ET during the growth periods of 2015 were generated by the methodologies illustrated above. Totally 36 cloud-free days were selected to generate daily ET and ET_0F . Then the simulated daily ET_0F were employed to extrapolate ET for all cloudy days. Continuous daily ET estimates were compared with ground measurements at the Daman and Huazhaizi stations. Also, the outputs of METRIC including sensible heat flux (H_{inst}) and instantaneous latent heat flux (λET_{inst}) were compared with the ground measurements. Note that some observed fluxes could not be measured due to bad weather conditions or to instrument failure.

The scatter plots in Figure 2 show the comparison between measured and modelled instantaneous heat flux including H_{inst} and λET_{inst} . The values of the coefficient of determination (R^2), root-mean-square error (RMSE), and mean absolute percentage error (MAPE) between the HJ1B-retrived and EC-observed H_{inst} were 0.93, 15.63 Wm^{-2} , and 11.7% respectively. It was suggested a good agreement between simulated and measured H_{inst} . However, METRIC underestimated H_{inst} values when these were compared with the eddy covariance measured

values and the slope for the linear regressions is 0.87 which is less than 1. R^2 , RMSE and MAPE between measured and modelled λET_{inst} were 0.86, 24.17 Wm^{-2} and 13.8% respectively, indicating a good performance in estimating λET by HJ-1 data through METRIC. Corresponding to the underestimation of H_{inst} , METRIC also overestimated λET_{inst} values when compared with ground measurements. The underestimation of H and overestimation of λET compared with the ground measurements were confirmed and the slopes for line regression were 0.87 and 1.13. Li et al. (2015) and Huang et al. (2015) found the RS-based surface energy balance models may overestimate ET due to the underestimation of sensible heat flux in arid and semiarid regions where water limiting situation is prevailing [32, 33]. Integrating the information of soil moisture into METRIC may be considered in the future.

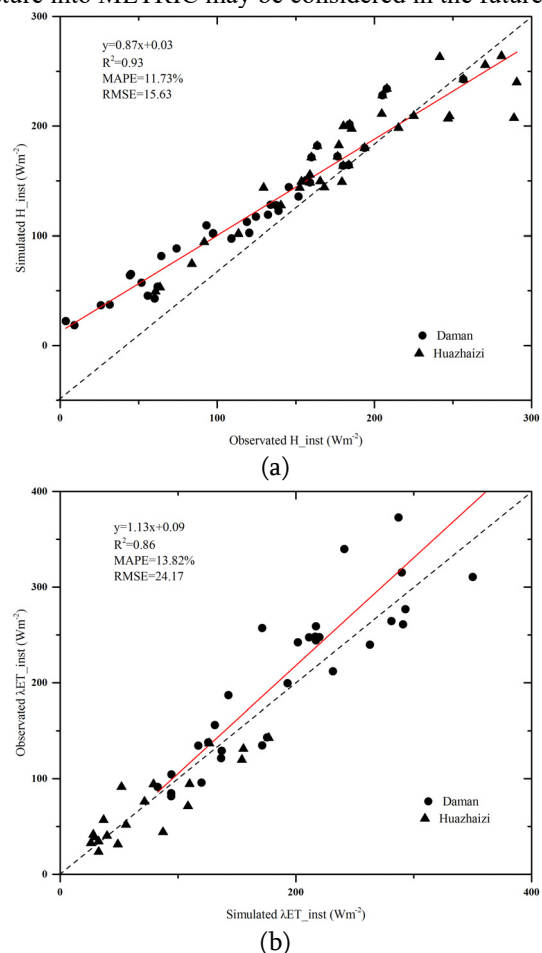


Figure 2. Scatter plots of (a) HJ-retrieved and EC-observed instantaneous sensible heat flux (H_{inst}) and EC system; (b) HJ-retrieved and EC-observed instantaneous latent heat flux (λET_{inst}).

For the Daman station (cropland) in Figure 3(a), R^2 is 0.95, indicating a strong correlation between estimated and measured daily ET. And MAPE and RMSE are 0.31 $mm d^{-1}$, and 12.04%, respectively, again suggesting good performance. The larger absolute difference (AD) occurred in the images of 6 June (1.85 $mm d^{-1}$ of AD) and 8 August (2.14 $mm d^{-1}$ of AD). The overestimation of latent heat flux (λET) and the missing 30-min data in EC system might explain the big errors. In addition, the simulated ET was overestimated compared with EC

measurements during mid-September and late September when the field was covered by maize residue, Odhiambo and Irmak (2012) also reported similar overestimation results of ET because of soybean residues. Figure 3(a) indicates that the continuous daily ET method with HJ-1 data captured the similar dynamics of daily ET as field measurements. Daily ET showed an increasing trend after early May and a decreasing trend since September and varied from 0.27 mmd^{-1} to 7.51 mmd^{-1} . There was always an impermanent increase after rainfall and irrigation events in the maize growth period, such as days after rain including 15 May (DOY 136), 5 June (DOY 157), 20 June (DOY 172), 5 July (DOY 187), 24 August (DOY 237), 3 September (DOY 247), and 19 September (DOY 263) and days after irrigation including 24 April (DOY 115), 18 May (DOY 139), 31 May (DOY 152), 7 June (DOY 159), 11 July (DOY 193), and 8 August (DOY 221). Rain events influenced ET because of the decreased water vapor pressure deficit (VPD), which caused temporal activation of the stomata, thus leading to the expedition of transpiration [34]. Rain and irrigation also increased the soil moisture, which would reduce soil resistance and soil water stress so that ET increased [16]. For the Huazhaizi station (sandy desert), R^2 , RMSE and MAPE were respectively 0.89, 0.16 mmd^{-1} and 13.2%, indicating a strong correlation between measured and modelled ET. Most of the time daily ET stayed fairly low and was less than or around 1 mm. The maximum of ET occurred after intensive rainfall from June 29 (DOY 181) to July 8 (DOY 190), during which there was intense rainfall.

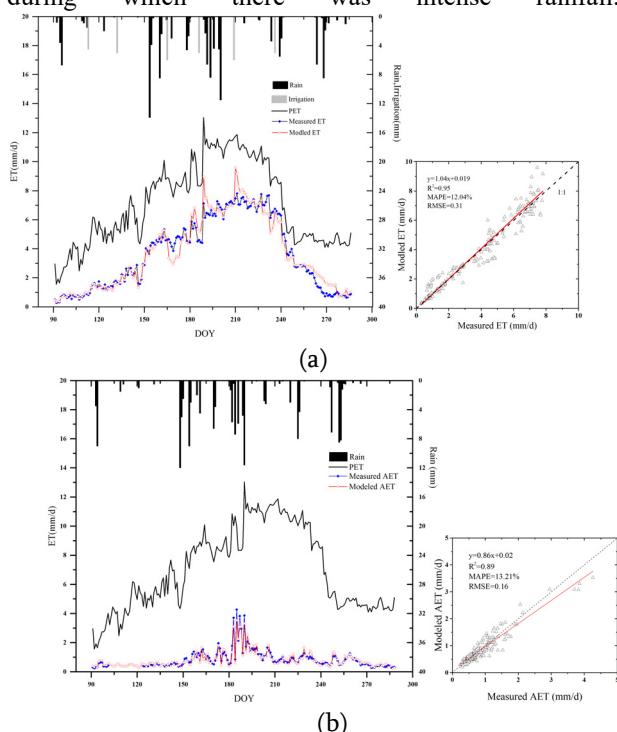


Figure 3. Comparison of time series of daily ET measured by the EC system and estimated through model over growth period in 2015 at (a) Daman station and (b) Huazhaizi station. ET_0 derived from meteorological data was also shown here in black line.

3.2 Assessing the Performance of HJ-derived ET_0F

Continuous daily ET_0F were obtained through the cubic interpolation method with available HJ-1 images. The temporal patterns of the variables with HJ-derived ET_0F , NDVI, LAI and soil moisture (SM) of 10 cm were plotted in Figure 4. Compared with the Landsat-derived ET_0F , HJ-derived ET_0F could fit the characteristics of ET_0F better. At the Daman Station, ET_0F derived from HJ-1 showed an increasing trend since the beginning of the growing season (late April) and a decreasing trend since the starting of the non-growth season, especially the harvesting season in mid-September. The ET_0F was around 0.2 in the early April, then gradually increased and could reach 0.72 in the ripe period of maize in August. The ET_0F spikes always occurred after rain and irrigation, such as the peaks on 5 April (DOY 96), 15 May (DOY 136), 5 June (DOY 157), 20 June (DOY 172), 8 August (DOY 221), and 24 August (DOY 237). Obviously, Landsat 8 with 16-day revisit period (only one image per month due to cloud) could hardly capture the dynamic change, thus resulting in large uncertainties. The results in Figure 5 demonstrated the good agreement between the fitted and EC-measured ET_0F with the R^2 of 0.89, MAPE of 12.97%, and RMSE of 0.065.

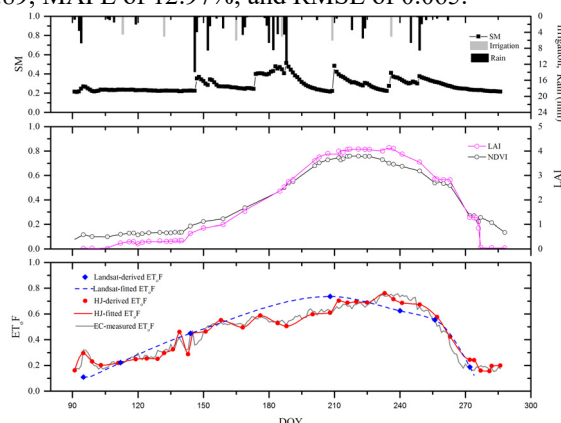


Figure 4. Time series variation of ET_0F , NDVI, LAI and SM at Daman station.

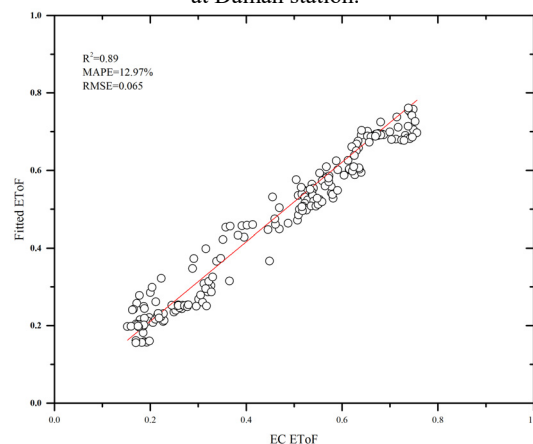


Figure 5. Scatter plots of fitted ET_0F and EC-measured ET_0F at Daman station.

3.3 Spatial and Temporal Variability of Daily ET over Agriculture Land

The mean and standard deviation of daily ET over different land use type from April was illustrated in Figure 6. The mean represented the average strength of ET, whereas the standard deviation illustrated the degree of its spatial variability in the experimental region. A smaller value of the standard deviation (short error bar) signified a more uniform spatial ET distribution. On the contrary, a larger value of the standard deviation (long error bar) means a more heterogeneous spatial ET distribution. Also, the spatiotemporal variability of ET for the whole experimental area can be seen more easily and clearly exhibited from the sum of daily ET for every month during crop growth period than day-by-day ET from April to September (Figure 7).

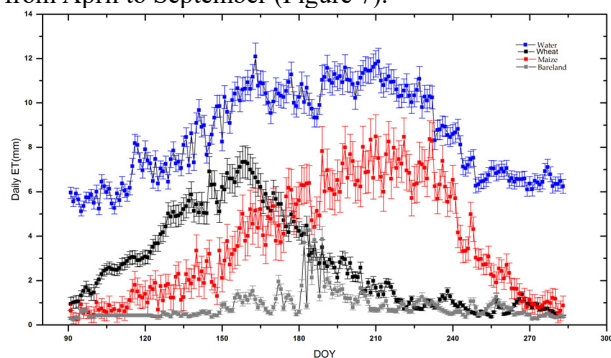


Figure 6. The spatial mean value of daily ET for four typical land use including maize, wheat, bare land and water. Error bar are standard errors of daily ET.

The high daily ET values represented well-irrigated wheat parcels in April and May, when winter wheat was in the tillering or jointing stage and maize was in the seeding stage. As can be seen Figure 7, the pixels of wheat stayed an obviously higher value than maize. However, the mean values of daily ET for maize gradually increased from late April, the trend of which began to be different from that of bare land. In early-June, the spatial mean values of daily ET on wheat pixels reached up to 7.34mm, when winter wheat was in the heading stage. The daily ET for maize increased quickly and the spatial distribution of daily ET was discrete during vigorous growing jointing stages of maize, with the standard deviation can reach up to 1.01 mm (16.8% of the mean value). The pattern of daily ET in July is strongly linked to the crop planting structure. The high ET values occurred at well-irrigated maize parcels in mid-season growth stages. The spatial distribution of ET in July was more heterogeneous than that in June, with a standard deviation of 1.67mm (25.3% of the mean value). The high spatial variability in the distribution of ET reflects different stages of crop growth and soil moisture conditions over the studied region. The daily ET at pixels of wheat planting parcels drastically decreased in July. Even the pattern of daily ET for wheat appeared to be similar to that for bare land from late July according to Figure 8. This was because winter wheat was already harvested and maize was in the heading stage, with NDVI for wheat less than 0.2 and that for maize around 0.65. The spatial mean values of daily ET for maize stayed steadily at high value in August when maize was in the mature stage. Maize harvesting in September caused a rapid decline in mean

of daily ET, to the mean of daily ET less than 2mm. Moreover, the trend of daily ET for maize and wheat was similar to that for bare land since September, staying at a low level (around 1mm). This indicated that daily ET for crops was closely related to soil condition during non-growing season. The spatial mean values of daily ET for water always stayed at absolute high level than other land use types. It showed an increasing trend since late April. Then a high evaporation intensity happened during July and August, with the peak up to 13.05 mm. Since September, the mean of daily ET for water also showed a decreasing trend. Conversely, bare land always stayed at a low evapotranspiration under low soil moisture condition and low vegetation coverage. But, ET for bare land would fluctuate with the increasing soil moisture after rain.

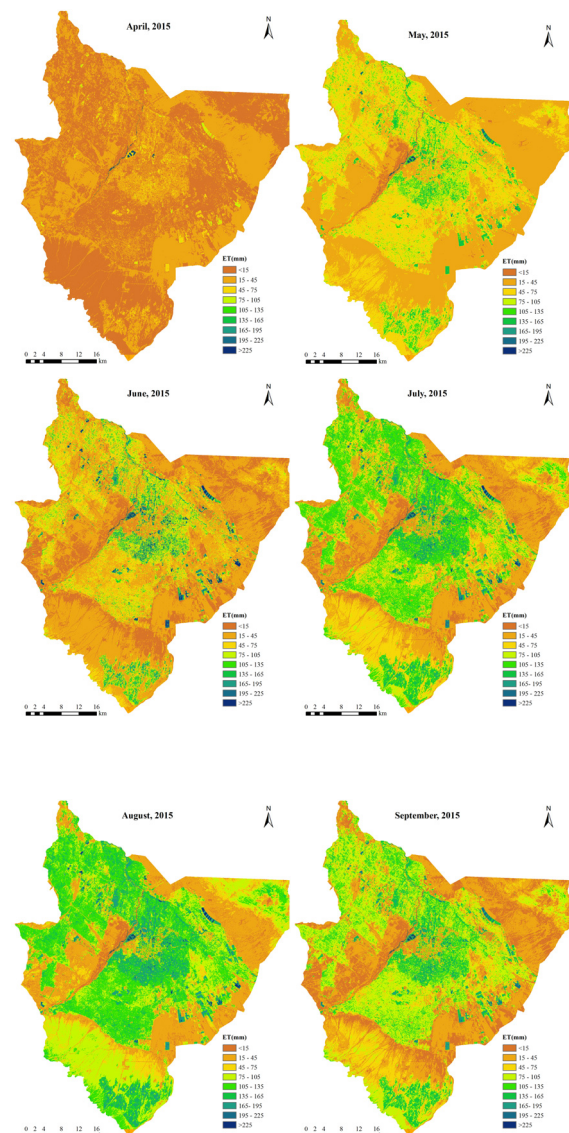


Figure 7. Spatial distribution of ET (mm) every month in the middle reach of HRB from April to September 2015.

Monthly spatiotemporal variation of ET over agriculture land during crop growth period can be seen in Figure 8. Similar seasonal dynamic trends were apparent for all plants in agriculture land, with ET increasing first to peak, and then decreasing. From April to May, all of the monthly ET values increased significantly as vegetation coverage. Wheat had the

highest monthly ET (86.2 mm) in April and reached up to 155.3 mm in May. Strong evapotranspiration capability and the large number of water supply ensured that the monthly ET values for maize and other plants reached their peak values in July and August. The ET values for unused bare land remained steady and low through whole growth period. ET values for all the land cover classes in agriculture land fell sharply with the onset of vegetation maturity or senescence since September.

4 Conclusions

A continuous daily ET at a high spatiotemporal resolution estimation is essential for growers in their efforts to apply the right amount of water at the right time. A method combining METRIC with f_c - T_{rad} space fed with HJ-1 data was used to convert satellites-retrieved ET on clear days into continuous time series daily ET. This study mapped continuous daily ET distribution in a representative area in the oasis of the HRB using the METRIC model and 36 HJ-1 images acquired during the growing season of 2012. The METRIC estimated surface energy flux and daily ET were compared with in situ measurements.

High accuracy was found by comparing the modelled results including instantaneous sensible heat flux (H), instantaneous latent heat flux (λ ET) and daily ET with the ground measurements. Our studies suggested that it was practicable and feasible to estimate continuous daily ET based on METRIC with f_c - T_{rad} space driven HJ-1 data. METRIC-based outputs agreed well with flux tower measured ET both instantaneously and at daily time step. High accuracy of daily ET was found during the growing season. Meanwhile, the fraction of potential ET (ET_0F) was derived from the available clear sky HJ-1 overpass dates using a cubic interpolation technique. HJ-1 with visit cycle at 2-4 days is more capable of capturing the dynamic variation of ET_0F than Landsat 8. The results demonstrated that HJ image data was very useful in estimating continuous daily ET for crops at the field scale. The present work supports the use of the remote sensing for simple, rapid, and relatively accurate estimation of daily ET at field scale and the water consumption for crops in every growth stage. Such accumulated values are critical, for example, for water use planning, irrigation scheduling and water management, especially in arid and semiarid areas.

However, error and uncertainty of HJ-derived estimates still exist. On the one hand, METRIC model itself has the uncertainty with variables/parameters in these equations varying with the domain scale, which would largely determine the mechanisms of error propagation and the magnitudes of errors in the resulting surface flux estimates. Second, optical remote sensing would always suffer from the clouds. When the HJ-available interval is more than 8 days, the fitted ET from HJ cannot catch the intensive change of ET caused by the rainfall and irrigation events, which often represent the change of weather and soil moisture conditions (Figure 4). In future, while work is done to enhance

model, a combination of HJ and other high temporal resolution satellite image data such as MODIS should be considered. Moreover, the main factors controlling spatial and temporal variation of ET such as rain, irrigation, temperature, relative humidity, wind speed and soil moisture should be further examined.

References

1. Q. Zhang, V.P. Singh, P. Sun, X. Chen, X.C. Zhang, Z.X. Zhang, J.F. Li, Precipitation and stream-flow changes in China: changing patterns, causes and implications, *J. Hydrol.* **410**, 204-21 (2011)
2. Y.T. Yang, Evapotranspiration over heterogeneous vegetated surfaces models and applications, Springer Theses Recognizing Outstanding Ph.D. Research, Tsinghua University, Beijing, China (2015)
3. P. Bhandana, N. Lazarovitch, Evapotranspiration, crop coefficient and growth of two young pomegranate (*Punica granatum* L.) varieties under salt stress, *Agr. Water Manage.* **97**(5), 715-722 (2010)
4. B. Zhang, S. Kang, F. Li, L. Zhang, Comparison of three evapotranspiration models to Bowen ratio-energy balance method for a vineyard in an arid desert region of northwest China, *Agricultural and Forest Meteorology* **149**(10), 1629-1640 (2008)
5. D. Vickers, C.K. Thomas, J.C. Pettijohn, J. Martin, B.E. Law, Five years of carbon fluxes and inherent water-use efficiency at two semi-arid pine forests with different disturbance histories, *Tellus Series B: Chemical & Physical Meteorology*, **64** (8), 978-988 (2011)
6. W.G.M. Bastiaanssen, M. Menenti, R.A. Feddes, A.A.M. Holtslag, A remote sensing surface energy balance algorithm for land (SEBAL) 1. Formulation, *J. Hydrol.* **212-213**, 198-212 (1998)
7. Z. Su, The Surface Energy Balance System (SEBS) for estimation of turbulent heat fluxes, *Hydrology and Earth System Sciences* **6**, 85-99 (2002)
8. R.G. Allen, M. Tasumi, R. Trezza, Satellite-based energy balance for mapping evapotranspiration with internalized calibration (METRIC)-model, *J. Irrig. Drain. Eng.* **133**, 380-394 (2007)
9. G.B. Senay, S. Bohms, R.K. Singh, P.H. Gowda, N.M. Velpuri, H. Alemu, J.P. Verdin, Operational evapotranspiration mapping using remote sensing and weather datasets: A new parameterization for the SSEB approach, *J. Am. Water Resour. Assoc.*, **49**, 577-591 (2013)
10. W.P. Kustas, J.M. Norman, A two-source approach for estimating turbulent fluxes using multiple angle thermal infrared observations, *Water Resource Research* **33**, 1495-1508, (1997)
11. M.C. Anderson, J.M. Norman, G.R. Diak, W.P. Kustas, J.R. Mecikalski, A two-source time-integrated model for estimating surface fluxes using thermal infrared remote sensing, *Remote Sensing of Environment* **60**, 95-216, (1997)

12. J.D. Kalma, T.R. McVicar, M.F. McCabe, Estimating land surface evaporation: a review of methods using remotely sensed surface temperature data, *Surveys in Geophysics* **29**, 421-469 (2008)
13. S. Liang, K. Wang, X. Zhang, M. Wild, Review on estimation of land surface radiation and energy budgets from ground measurement, remote sensing and model simulations, *IEEE Journal of Selected Topics in Applied Earth Observations and Remote Sensing* **3**(3), 225–240 (2010)
14. A. Kilic, R.G. Allen, R. Trezza, I. Ratcliffe, B. Kamble, C.W. Robison, D. Ozturk, Sensitivity of evapotranspiration retrievals from the METRIC processing algorithm to improved radiometric resolution of Landsat 8 thermal data and to calibration bias in Landsat 7 and 8 surface temperature, *Remote Sensing of Environment* **185**, 198-209 (2016)
15. P.H. Gowda, J.L. Chavez, P.D. Colaizzi, S.R. Evett, T.A. Howell, ET mapping for agricultural water management: Present status and challenges, *Irrig. Sci.* **26**, 223–237 (2008)
16. A.P. Teresa, P. Isabel, C. Mario, C. Jose, L.S. Francisco, P. Paula, S.P. Luis, Evapotranspiration and crop coefficients for a super intensive olive orchard: An application of SIMDualKc and METRIC models using ground and satellite observations. *Journal of Hydrology* **519** (B), 2067-2080 (2014)
17. J.P. Burkhalter, T.C. Martin, R.G. Allen, J. Kjaersgaard, E. Wilson, R. Alvarado, J.S. Polly, J.S. Estimating crop water use via remote sensing techniques vs. conventional methods in the South Platte River basin, Colorado, *Journal of the American Water Resources Association* **49** (3), 498-517. (2013)
18. S.R. Evett, W.P. Kustas, P.H. Gowda, M.C. Anderson, J.H. Prueger, T.A. Howell, Overview of the Bushland Evapotranspiration and Agricultural Remote sensing EXperiment 2008 (BEAREX08): A field experiment evaluating methods for quantifying ET at multiple scales, *Advances in Water Resources* **50**, 4-19 (2012)
19. M.C. Anderson, R.G. Allen, A. Morse, W.P. Kustas, Use of Landsat thermal imagery in monitoring evapotranspiration and managing water resources, *Remote Sensing of Environment* **122**, 50-65 (2012)
20. K.A. Semmens, M. Anderson, W.P. Kustas, M. Velez, Monitoring daily evapotranspiration over two California vineyards using Landsat 8 in a multi-sensor data fusion approach, *Remote Sensing of Environment* **185**(185): 155-170 (2015)
21. C. Hu, P. Tang, Automatic algorithm for relative radiometric normalization of data obtained from Landsat TM and HJ-1A/B charge-coupled device sensors, *J. Appl. Remote Sens.* **6**, 063509 (2012)
22. X.Y. Ouyang, L. Jia, G.C. Hu, Retrieval of land surface temperature over the Heihe River Basin using HJ-1B thermal infrared data, *Remote Sensing* **7**, 300-318 (2014)
23. R. Zhang, R. Sun, J.P. Du, T.L. Zhang, Y. Tang, H.W. Xu, S.T. Yang, W.G. Jiang, Estimations of net primary productivity and evapotranspiration based on HJ-1A/B data in Jinggangshan City, China, *Journal of Mountain Science* **10**, 777–789 (2013)
24. W.Z. Zhao, B. Liu, The response of sap flow in shrubs to rainfall pulses in the desert region of China, *Agricultural and Forest Meteorology* **150**, 1297-1306 (2010)
25. X.J. Wu, J. Zhou, H.J. Wang, Y. Li, B. Zhong, Evaluation of irrigation water use efficiency using remote sensing in the middle reach of the Heihe river, in the semi-arid Northwestern China, *Hydrological Processes* **29** (9), 2243-2257 (2014)
26. Z.W. Xu, Y.F. Ma, S.M. Liu, W.J. Shi, J.M. Wang, Assessment of the energy balance closure under advective conditions and its impact using remote sensing data, *Journal of applied meteorology and climatology* **56**, 127-140 (2017)
27. S.M. Liu, Z.W. Xu, W.Z. Wang, Z.Z. Jia, M.J. Zhu, J.W. Bai, J.M. Wang, A comparison of eddy-covariance and large aperture scintillometer measurements with respect to the energy balance closure problem, *Hydrology and Earth System Sciences* **15** (4): 1291–1306 (2011)
28. B. Zhong, A.X. Yang, A.H. Nie, Y.J. Yao, H. Zhang, S.L. Wu, Q.H. Liu, Finer resolution land-cover mapping using multiple classifiers and multisource remote sensed data in the Heihe river Basin, *IEEE Journal of Selected Topics in Applied Earth Observations and Remote Sensing* **8** (10), 4973-4992 (2015)
29. N. Bhattarai, L.J. Quackenbush, J. Im, S.B. Shaw, A new optimized algorithm for automating endmember pixel selection in the SEBAL and METRIC models, *Remote Sensing of Environment* **196**, 178-192 (2017)
30. R.G. Allen, R. Trezza, M. Tasumi, J. Kjaersgaard, J. *Mapping Evapotranspiration at High Resolution Using Internalized Calibration: Application Manual for Landsat Satellite Imagery; Version 3.0.*, Kimberly, University of Idaho (2014)
31. D. Long, V.P. Singh, A modified surface energy balance algorithm for land (M-SEBAL) based on a trapezoidal framework, *Water Resources Research* **48**, W02528 (2012)
32. Y. Li, J. Zhou, H.J. Wang, D.Z. Li, Y.Z. Zhou, Q.G. Zhou, Integrating soil moisture retrieved from L-band microwave radiation into an energy balance model to improve evapotranspiration estimation on the irrigated oases of arid regions in northwest China, *Agricultural and Forest Meteorology* **214–215**, 306–318 (2015)
33. C.L. Huang, Y. Li, J. Gu, L. Lu, X. Li, Improving Estimation of Evapotranspiration under Water-Limited Conditions Based on SEBS and MODIS

Data in Arid Regions. *Remote Sensing* **7**, 16795–16814 (2015)

34. I. Baker, L. Prihodko, A. Denning, M. Goulden, S. Miller, H. Da Rocha, Seasonal drought stress in the Amazon: reconciling models and observations. *Journal of Geophysical Research Biogeosciences* **113** (G1), 212-221 (2015)